JOURNAL OF MATERIALS SCIENCE **39** (2004) 5939–5949

Designing for ultrahigh-temperature applications: The mechanical and thermal properties of HfB_2, HfC_x, HfN_x and αHf(N)

E. WUCHINA, M. OPEKA
Naval Surface Warfare Center, W. Bethesda, MD, USA
E-mail: wuchinaej@nswccd.navy.mil

S. CAUSEY
Southern Research Institute, Birmingham, AL, USA

K. BUESKING
Materials Research & Design, Philadelphia, PA, USA

J. SPAIN, A. CULL
Southern Research Institute, Birmingham, AL, USA

J. ROUTBORT
Argonne National Laboratory, Argonne, IL, USA

F. GUITIERREZ-MORA
University of Seville, Seville, Spain

The thermal conductivity, thermal expansion, Young's Modulus, flexural strength, and brittle-plastic deformation transition temperature were determined for HfB_2, $HfC_{0.98}$, $HfC_{0.67}$, and $HfN_{0.92}$ ceramics. The mechanical behavior of αHf(N) solid solutions was also studied. The thermal conductivity of modified HfB_2 exceeded that of the other materials by a factor of 5 at room temperature and by a factor of 2.5 at 820°C. The transition temperature of HfC exhibited a strong stoichiometry dependence, decreasing from 2200°C for $HfC_{0.98}$ to 1100°C for $HfC_{0.67}$ ceramics. The transition temperature of HfB_2 was 1100°C. Pure HfB_2 was found to have a strength of 340 MPa in 4 point bending, that was constant from room temperature to 1600°C, while a $HfB_2 + 10\%\ HfC_x$ had a higher room temperature bend strength of 440 MPa, but that dropped to 200 MPa at 1600°C. The data generated by this effort was inputted into finite element models to predict material response in internally heated nozzle tests. The theoretical model required accurate material properties, realistic thermal boundary conditions, transient heat transfer analysis, and a good understanding of the displacement constraints. The results of the modeling suggest that HfB_2 should survive the high thermal stresses generated during the nozzle test primarily because of its superior thermal conductivity. The comparison the theoretical failure calculations to the observed response in actual test conditions show quite good agreement implying that the behavior of the design is well understood. © *2004 Kluwer Academic Publishers*

1. Introduction

Structural materials for use in high-temperature oxidizing environments are presently limited to SiC, Si_3N_4, oxide ceramics, and composites of these materials. The maximum use temperatures of silicon-based ceramics is limited to ≈1600°C due to the onset of active oxidation and lower temperatures in water vapor environments, while oxides have exhibited high creep rates at higher temperatures. The development of structural materials for use in oxidizing and rapid heating environments at temperatures above 1600°C is therefore of great engineering importance.

Hafnium and zirconium-based ceramics (carbides, borides, and nitrides) display a number of unique properties, including extremely high melting temperature and hardness, as well as high thermal and electrical conductivity and chemical stability. This combination of properties make these materials potential candidates for a variety of high-temperature structural applications, including engines, hypersonic vehicles, plasma arc electrodes, cutting tools, furnace elements, and high temperature shielding. The present investigation describes the thermal and mechanical behavior of HfB_2, HfC, and HfN ceramics synthesized by reactive hot pressing.

For structural design purposes, the thermomechanical properties of candidate materials must be fully characterized because a major concern for design is thermal cycling that can result in the thermal-stress failures. Knowledge of the ductile-to-brittle-transition temperature is necessary for thermostructural analysis and advanced design. Since some plasticity may be desirable, the investigation of materials with melting temperatures greater than 2000°C that possess room temperature ductility became another goal of the program. With this in mind, in addition to investigating the pure hafnium-based ceramics, interest in the Hf-N system extended the scope of the program into the Hf-N solid solutions. It is known that interstitial nitrogen increases the melting temperature [1] of the α-Hf single-phase material (according to the Hf-N equilibrium diagram), as well as increases hardness [2]. The Hf-C system has a more limited solubility range, and a less dramatic effect on melting temperature. Boron and oxygen also have limited solubility [3–5], and an increase in melting temperature of αHf is not observed in those systems.

2. Design issues

Ultra-high temperature materials, or UHTCs, are not a new class of materials. In the 1960s and early 1970s, there was a large amount of work, mostly sponsored by the Air Force, to study the thermochemistry, phase equilibria, and oxidation behavior of transition-metal borides, carbides, and nitrides [6–9]. One of the major outcomes of this work was the identification of the HfB_2-SiC material as a good high-temperature oxidation-resistant material. Along with recent work, most experimental studies published have focused on oxidation behavior [10–16]. The mechanical behavior, specifically the high-temperature mechanical properties, has not been widely reported. In this paper, the flexural properties of HfB_2, ZrB_2, HfC_x, HfN_x and αHf(N) will be discussed.

The oxidation studies have been widely successful, and much insight has been gained into the mechanisms and behavior of these materials as a function of temperature, gas chemistry, and total pressure. But for most applications, a static, unloaded surface is not possible—some mechanical force will act upon the exposed structure—most often at elevated temperature. This force may not only be applied externally, but can be generated internally as a function of the heating process—thermal stresses generated through thickness. These loads can often be quite high, and are a function of the intrinsic material properties. Therefore, it is important to know the room temperature strength of the material, the strength at peak temperature, the coefficient of thermal expansion (CTE), and the thermal conductivity as a function of temperature. As important as knowing the material properties, it is equally important to understand the application needs, and to be able to produce accurate thermostructural models for the use conditions. When designing for high-temperature applications, it is not enough to know the melting temperature and oxidation behavior. These are engineering materials, and a thermomechanical property database needs to be developed before a designer or engineer will consider these materials. When will peak loads occur? Will flexure tests accurately reflect failure modes? What is the temperature at that point? Obviously, the modulus and strength of these materials will change as a function of temperature. It is well understood by the materials science community that microstructure and composition affect not only the oxidation behavior of the material, but its strength as well. However, purity of the raw materials, contamination by milling media, and the addition of sintering aids and alloying agents to alter the oxidation behavior, will affect not only the room-temperature strength of the material, often in a positive fashion, but will likely drastically reduce the high-temperature mechanical properties. It is for this reason that NSWCCD has focused on pure and mixed-phase materials without oxide sintering aids or silicon carbide and silicon nitride additions. These second phases often reside at grain boundaries, and do not have the same melting or bonding behavior as the UHTC material, leading to reduced strength and modulus at temperature. For longer-term applications, creep may be a problem. The issue of high room temperature strength versus the need to maintain high strength at temperature is a design consideration, and obviously the materials can be tailored to allow each. In this paper, the discussion of HfB_2 (Generation 1—pure HfB_2 versus Generation 2—$\text{HfB}_2 + 10\%\ \text{HfC}_x$) focuses on this issue.

3. Experimental procedure

The materials tested were HfB_2 (pure and modified with Hf and HfC), HfC_x ($x = 0.67$ and 0.98), HfN, and αHf-N solid solutions. The billets were hot-pressed (2000–2500°C, 20–30 MPa) at NSWCCD and Hi-Z Technologies (San Diego, CA)), and were machined into tests specimens by electrical discharge machining (EDM) techniques and tested at Southern Research Institute (Birmingham, AL). A example cutting plan for excising test specimens from a hot-pressed billet is shown in Fig. 1. The hafnium-based compounds were hot-pressed from −325 mesh powders from Cerac, Inc. The non-stoichiometric $\text{HfC}_{0.67}$ ceramics were prepared according to the reaction:

$$67\text{HfC} + 33\text{HfH}_2 \mid 100\text{HfC}_{0.67} + 33\text{H}_2.$$

For producing αHf-N, Hf and HfN powders were similarly blended into batches correlating to 2, 5, 10, 20, and 30 atomic percent N. The materials were densified by isothermal heat treatments of powder compacts at temperatures of 1300–2300°C in vacuum and under 1 atmosphere of helium.

All materials were characterized by density (Archimedes method and helium pychnometry), phase composition (X-ray diffraction using a Siemens Theta-Theta Diffractometer), and microstructure using a Jeol JSM-6400V Scanning Electron Microscope (SEM). For lattice parameter calculations in the HfC substoichiometric materials, an internal silicon standard was used.

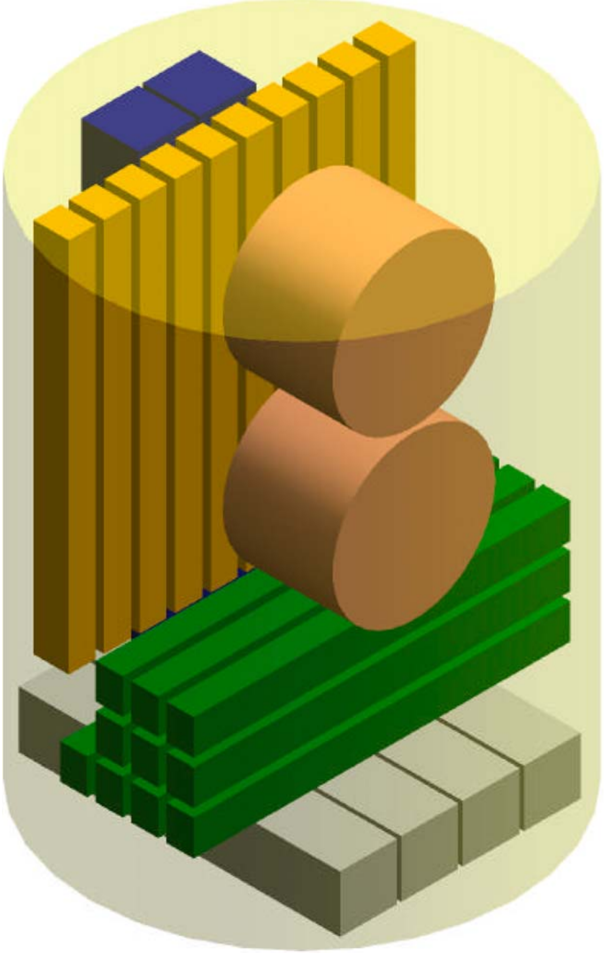

Figure 1 Typical cutting plan for excising test specimens.

The mechanical and thermal properties were evaluated, including elastic moduli, tensile strength, flexural strength, brittle-to-ductile transition temperature (BDT), thermal conductivity, and thermal expansion (CTE). The thermal conductivity of the materials was measured (sample size: 1.91 cm diameter × 1.27 cm thick) using a comparative rod technique, comparing the conductivity of a specimen with the conductivity of a reference (iron and stainless steel for this effort). The thermal conductivity was calculated from the heat flow and temperature difference across a known gage length within the specimen at a given thermal input. The CTE was measured (sample size: 0.64 cm diameter × 5.08 cm long) up to 2500°C using two different dilatometers: a quartz-rod dilatometer provided data up to 1000°C, and a graphite dilatometer was used up to 2500°C. The same specimens were used for both temperature ranges. The tensile test of ring specimens (4.57 cm OD × 4.06 cm ID × 1.27 cm) utilized an internal, inflatable membrane to apply hydrostatic pressure. The top and bottom enclosure plates and annular retaining rings were used to ensure that the loading was applied in the radial direction. Room and elevated temperature flexural tests were conducted (sample size: 0.30 cm × 0.635 cm × 4.318 cm) to determine strengths, moduli, and BDTs. Flexural testing was conducted over a wide temperature range to determine the transition from elastic stress-strain behavior to elastic plus plastic deformation. The BDT was determined from the change in slope of the load-deformation curve. The elastic moduli were determined using three techniques: the measurement of ultrasonic velocity, and the σ-ε slope from tensile ring and 3-point flexural tests.

The αHf-N samples were machined, ground, and polished to 5 × 5 × 12 mm size for compressive testing. Tests were carried out at constant crosshead speeds in an Instron Model 1125 Universal Tester fitted with a furnace and a muffle tube for controlled atmosphere, as described by Routbort [17]. The temperature range for these experiments was from room temperature to 1000°C, and the strain rates were 10^{-6} to 10^{-3}s^{-1}. Room-temperature tests were conducted in air; the higher-temperature tests were conducted in static argon for the pure Hf samples and in static N_2 for the Hf-N samples

4. Results and discussion

All materials tested were well densified. Fig. 2 shows the microstructure of the materials. HfB_2 (2a) has a fine-grained structure, with an average grain size of 10–20 μm, while $HfN_{0.92}$ has a larger grain size (40–60 μm). Both materials exhibit intergranular fracture characteristics. The microstructure of the hafnium carbide ceramics showed a substantial dependence on carbon content. The $HfC_{0.67}$ ceramics (2c) consisted of very large crystallites (>200 μm), while $HfC_{0.98}$ (2d) has a finer grain size (40–60 μm). The carbides also exhibited distinctly different fracture behavior. The $HfC_{.067}$ showed extensive intergranular fracture, while $HfC_{0.98}$ failed in an transgranular fracture mode, as seen by the flatter fracture surface. The $HfN_{0.92}$, $HfC_{0.98}$ and $HfC_{0.67}$ ceramics were all single phase. The measured lattice parameters of $HfC_{0.98}$ and $HfC_{0.67}$ were 4.64331 and 4.62368 Å, respectively, correlating well with those reported in the literature [18].

For the newer Generation 1 (as-received HfB_2, –325 mesh powder from Cerac, Inc. hot pressed at 2150°C) and Generation 2 HfB_2 (HfB_2 + 5%Hf + 4%C, also hot pressed at 2150°C), the microstructures were typically fine grained, with the HfC_x phase residing at the grain boundaries of the Generation 2 material. This reaction process was envisioned to produce a ductile grain boundary phase at lower temperature to enhance densification, and form a more refractory HfC_x at the final processing temperature. The need for improved densification became important when scaling up to larger billet sizes. For larger diameter molds, the increase in mold contact area, especially in taller billets, made uniform densification immensely more difficult. To overcome this, higher processing temperatures or pressures were generally needed. With graphite tooling, the limitation for pressure was determined to be 20 MPa. Pressing at higher temperatures generally leads to grain growth, which lowers strength.

Sintering studies in the Hf-N system showed that compositions containing less than 10% N could be fully densified at temperatures below 1500°C in a tungsten furnace under 1 atmosphere of helium. Hot pressing these materials in graphite dies and a carbon-element furnace induced rapid grain growth and carbon

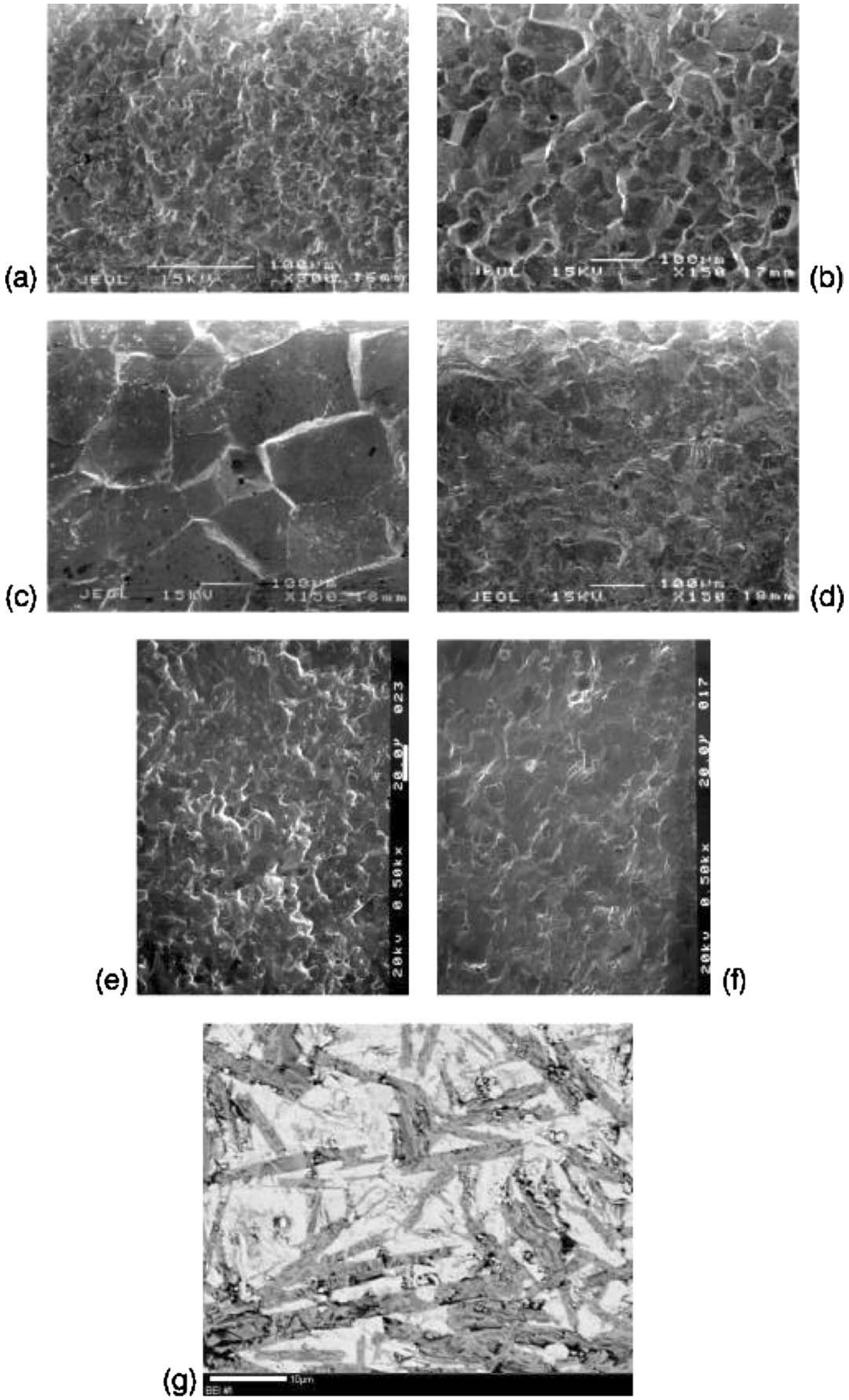

Figure 2 SEM micrographs of (a) HfB_2, (b) HfN0.92, (c) $HfC_{0.67}$, (d) $HfC_{0.98}$, (e) HfB_2 (Generation 1), (f) HfB_2 (Generation 2), and (g) Hf-17N-30B.

contamination, both of which contributed to producing low-strength, brittle materials. Microstructural examination also revealed a finer grain structure in the sintered materials than in the hot-pressed materials. All αHf(N) materials tested and described in this paper were produced by pressureless sintering techniques.

4.1. Thermal and mechanical testing results

The results of the flexural strength tests for Generation 1 and 2 HfB_2 are shown in Fig. 3. The HfB_2 (Generation 1) is considered the baseline material and has a room-temperature (RT) strength (4 point bending) of 340 MPa. The elevated temperature properties are

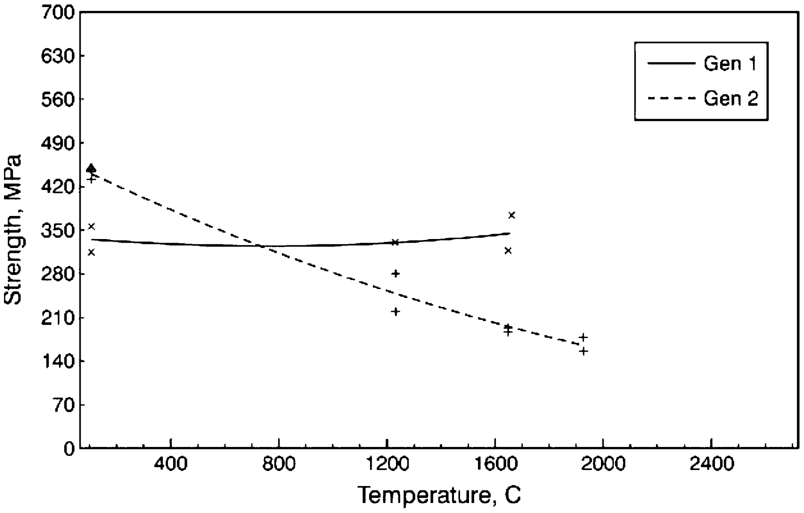

Figure 3 Bending strength of Generation 1 and Generation 2 HfB_2 as a function of temperature.

essentially unchanged up to 1600°C. The strength at room temperature of Generation 2 HfB_2 increased to 440 MPa, but was lowered to 200 MPa at 1600°C. It is believed that more exploratory work in this system could lead to an improvement to these poorer high temperature properties. The Hf-17N-30B material shown in Fig. 2g had a room temperature flexural strength of 240 MPa, but the strength dropped off quickly with temperature due to the presence of αHf(N). The HfC and HfN data is not shown due to the data scatter, but was lower than HfB_2 over the entire temperature range. This was likely due to the more covalent nature of the bonding in these materials, making them more difficult to uniformly densify.

The thermal conductivities of HfB_2, $HfC_{0.98}$, $HfC_{0.67}$, and $HfN_{0.92}$ are shown in Fig. 4. The conductivity of HfB_2 exceeded that of the other materials by a factor of 5 at room temperature and by a factor of 2.5 at 800°C. Additionally, the conductivity of HfB_2 decreased with temperature, while that of the other materials increased with temperature. Both the nitride and the carbides exhibited similar temperature coefficient of conductivity, but the conductivity of the $HfC_{0.98}$ exceeded that of the $HfC_{0.67}$ by a factor of two. The decreased thermal conductivity of the lower carbide can be explained by increased phonon scattering from carbon vacancies. The thermal expansion curves of the all four materials were quite similar, as shown in Fig. 5. The expansion of all materials was nominally the same up to 1500°C, with a CTE calculated to be 7.7×10^{-6}/°C. Above 1500°C, the $HfN_{0.92}$ ceramics exhibited some increase in the expansion rate, likely due to the loss of N from the lattice. The thermal conductivity for the Generation 1 and Generation 2 HfB_2 materials are mosly the same to that shown for the HfB_2 in Fig. 4, except that the Generation 2 material was slightly lower owing to the presence of HfC.

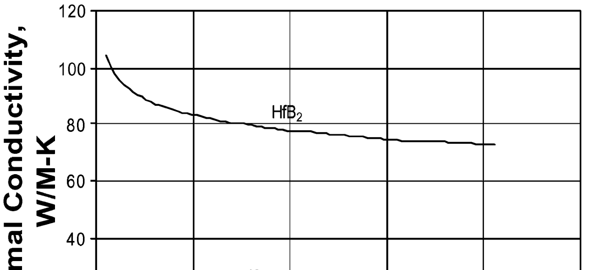

Figure 4 The thermal conductivities of HfB_2, HfN, $HfC_{0.67}$, and $HfC_{0.98}$.

Fig. 6 shows the flexural stress-deflection curves for HfB_2 at 1090 and 1230°C. At 1090°C, almost purely elastic behavior was observed up to specimen failure. At 1230°C, however, the deflection includes a significant plastic deformation component. Two modulus values were calculated from this curve based on the elastic and plastic components. The initial modulus is the modulus of the linear elastic portion of the load-deflection curve, while the secondary modulus is the slope after yielding. All modulus data calculated from the flexural testing are shown in Fig. 7. For the $HfC_{0.98}$ sample, no plastic deformation was observed up to 2200°C, while the substoichiometric $HfC_{0.67}$ sample exhibited plastic deformation at 1090°C. This difference in behavior can be attributed both to the significant difference in microstructure (Fig. 2) and to the compositional difference in two materials. The HfB_2 ceramics exhibited plastic deformation at a much lower temperature than the $HfC_{0.98}$ ceramics.

The room temperature Youngs Moduli were determined by tensile testing, flexural testing, and ultrasonic velocity measurements. The tensile testing-based data show very good agreement with the data gained from the ultrasonic velocity measurements. The modulus data calculated from the flexural testing are approximately 15% lower for all four materials. The flexural test-based moduli were expected to be low, since the compliance of the load train is not accounted for in the calculation and it utilizes a short-span specimen. HfB_2 was found to have the highest modulus, while $HfC_{0.67}$ had the lowest.

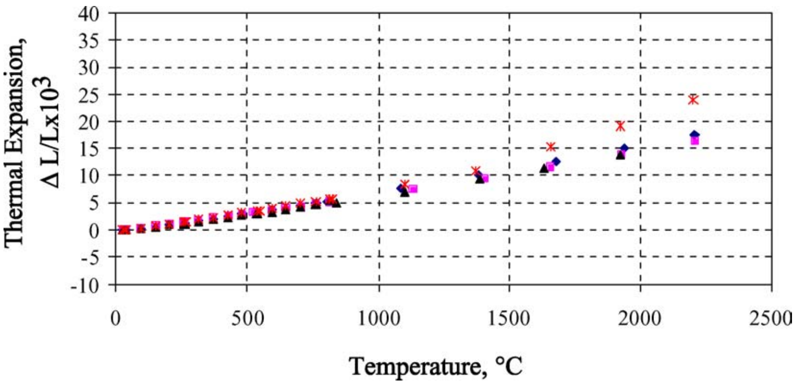

Figure 5 The thermal expansion of HfB_2, HfN, $HfC_{0.67}$, and $HfC_{0.98}$.

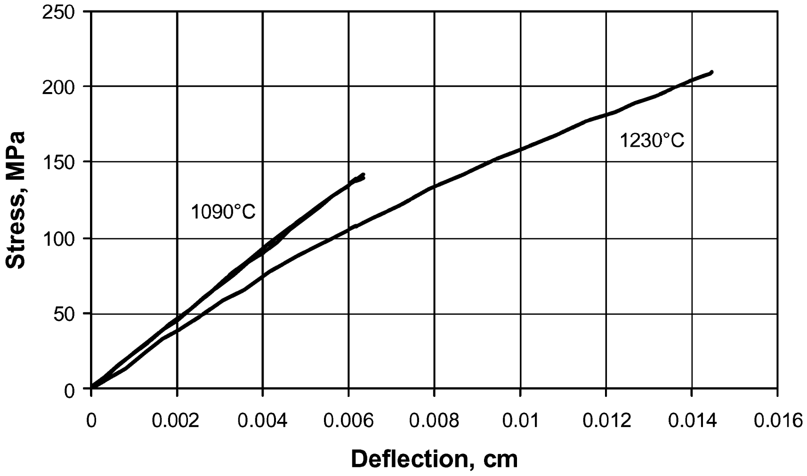

Figure 6 The flexural stress deflection curves for HfB_2 showing plastic behavior at 1230°C.

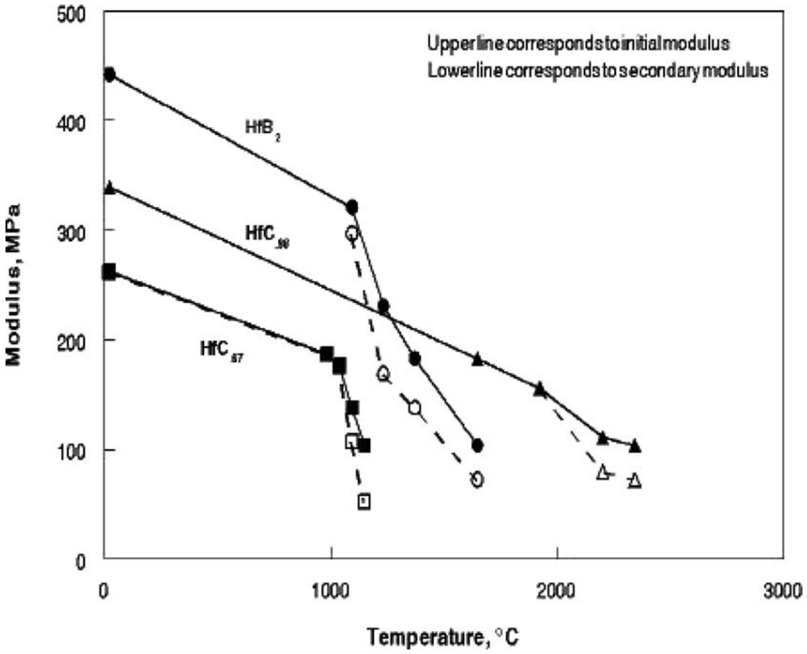

Figure 7 The modulus vs. temperature for HfB2, $HfC_{0.67}$, and $HfC_{0.98}$.

4.2. Hf-N materials—Results & discussion

The brittle-to-ductile transition (BDT) temperature for each composition is shown as a function of N concentration in Fig. 8. These tests were all conducted at a strain rate of 10^{-4} s^{-1}. The transition temperature was found to increase with N concentration. The BDT was observed at 400°C for Hf-2%N, but 1200°C for the Hf-30%N. The results of stress-strain (elastic plus plastic) measurements at room temperature at a constant strain rate ($\dot{\varepsilon}$) of 10^{-4} s^{-1} on various Hf-N solid solutions are shown in Fig. 9. The data indicated that fracture stress increased from ≈1000 MPa for Hf-2N to 1250 MPa

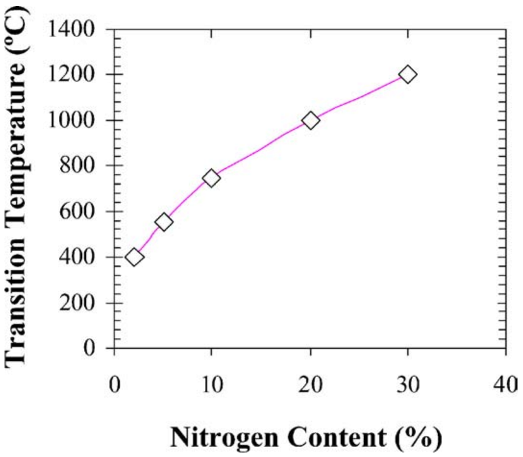

Figure 8 The brittle to ductile transition temperature for aHf(N) materials.

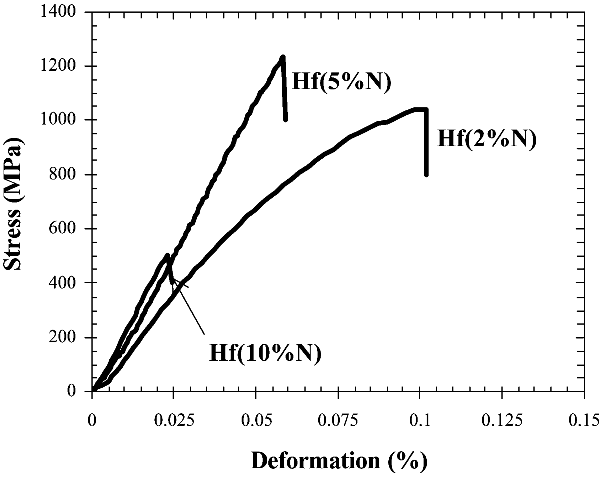

Figure 9 The stress-strain curves for aHf(N) materials.

for Hf-5N (and 800 MPa for pure Hf), but decreased to ≈500 MPa for Hf-10N. Therefore, at this strain rate at room temperature, the fracture stress exhibited a maximum at intermediate N concentration. By definition, fracture occurs when the fracture stress is lower than the flow stress: however, solute atoms and clusters affect the flow stress [3] and could also affect the surface energy by segregating to grain boundaries. This may modify the fracture energy. Therefore, it is possible that the maximum in room-temperature fracture stress observed for the Hf-5N alloys is a result of a combination of the two effects.

Stress-strain data for Hf-5N (strain rate of 10^{-4} s^{-1}) at a progression of temperatures are shown in Fig. 10. This composition exhibited brittle fracture at $T \leq$ 400°C, but deformed into a steady state (as indicated by the zero work-hardening rate) at higher temperatures. By definition, steady-state deformation was achieved above the BDT temperature for the Hf-2N, Hf-5N, and Hf-10N. Strain-rate-change experiments were performed, and the stress exponents derived from the experiments were between ≈5 and 8 for all compositions in the temperature range where the materials exhibited sufficient plasticity. It appears that the stress exponent for the solid solution could be slightly dependent on temperature, as the n-values tended to be higher at the lower temperatures, or could also be explained by the concept of a threshold stress. The limited ductility of some of the higher N content compositions precluded more detailed experiments. Fig. 11 presents limited data on the yield stress (defined as the intercept between the stress-vs.-strain curve at $\varepsilon = 0.002$) as a function of concentration, C = (% N). The data were obtained at 850°C, with $\dot{\varepsilon} = 10^{-4}$ s^{-1}. The fit to a $C^{1/2}$ was reasonable. The fact that yield stress in the Hf-N alloys correlated well with a $C^{1/2}$ fit strongly supports a model based on the effects of solid-solution hardening [19]. This fit was surprisingly good given that its underlying model is based on dilute solid solutions. We can only speculate that the dependence is the result of the cluster concentration rather than the concentration of the single N solute interstitials.

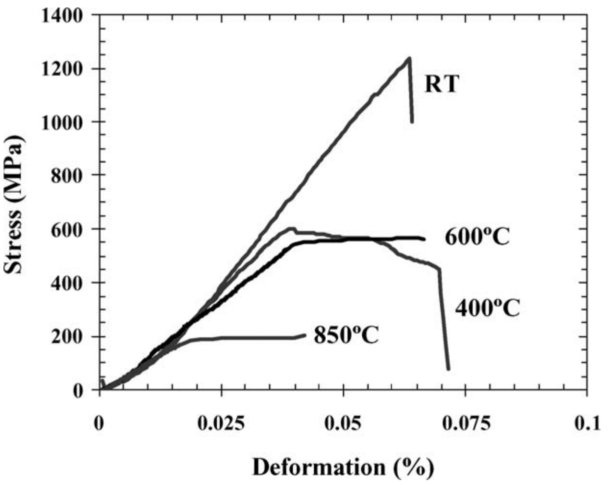

Figure 10 Stress-strain curves for Hf-5N.

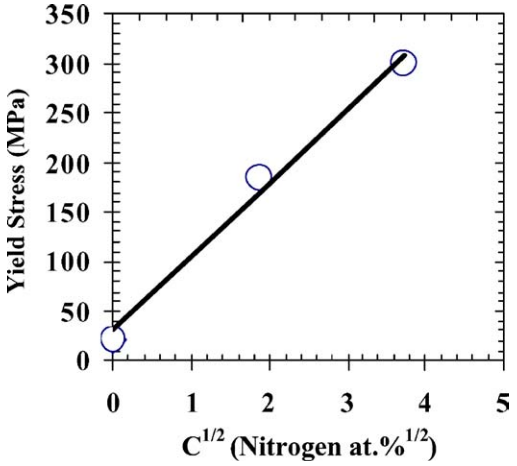

Figure 11 Yield stress as a function of concentration of nitrogen.

5. Design example

The thermomechanical response of HfB$_2$, HfC$_{.67}$, HfC$_{.98}$, and HfN$_{0.92}$ in an internally-heated nozzle geometry was analyzed. The material properties and thermal loads were inputted into the design tool derived from first principles [20–23] to evaluate the theoretical performance. Maximum stresses were calculated and compared to measured strengths to predict the

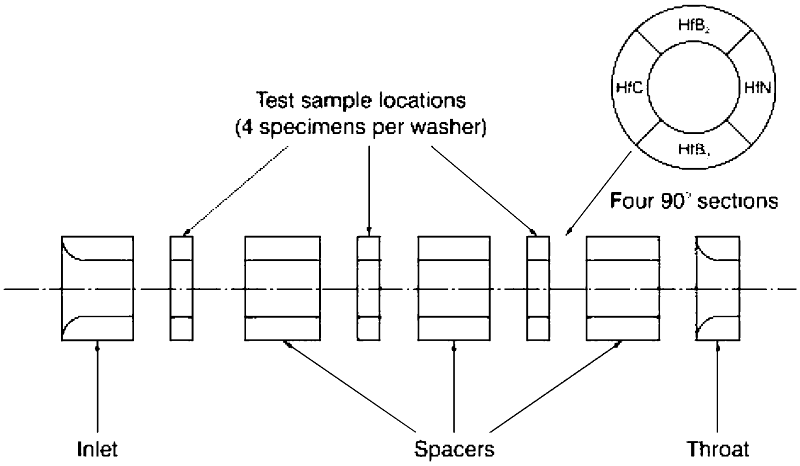

Figure 12 The sample configuration for nozzle test.

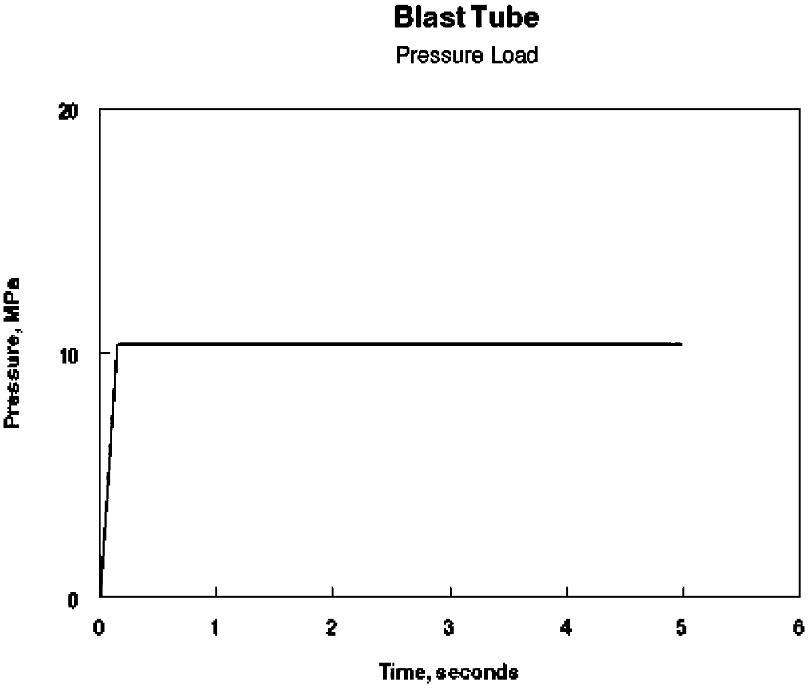

Figure 13 Typical pressure load profile for tests.

success or failure. Actual tests were carried out and compared to the simulated results. The specimen geometry used for the design model and nozzle tests is shown in Fig. 12. The test configuration is a cylindrical passage of washer-shaped test samples, and a throat section which was sized to control the pressure. The blast tube and location of the test samples includes individual 90° segments separated by graphite spacers. The pressure load profile applied to the sample is shown in Fig. 13. Gas temperatures of 2000 and 2400°C and pressures of 2.7 and 10.3 MPa were used for the study. The thermal conductivities, moduli, thermal expansion, and strength of the four materials used in the model are shown in Fig. 14 (in bar graph form).

A detailed finite element mode was used to investigate the stress state. The model employs the computed temperature field at the time of peak gradient in a 90° specimen. The displacement boundary conditions, which are critical to the solution, include radial constraint at the two outer corners, as shown. These constraints represent the outer motor case that restrains the test samples from moving outward at the corners but allows the middle section of the specimen to bend inward under the influence of the thermal gradient. The hoop constraint at the inner diameter prevents rigid body motion. The thermal gradient imposed on this design at 2000°C is shown in Fig. 15.

The maximum principal stresses resulting from this analysis shows a peak tensile value in the middle of the specimen. This stress field is a result of several mechanisms. Since the specimen is a 90° arc, the hoop stresses must go to zero at the free surfaces ($\theta = 0°$ and $\theta = 90°$). The thermal gradient will therefore induce a bending moment creating compression at the outer diameter and tension at the inner diameter. The superposition of these stresses results in the distribution shown in Fig. 16.

Fig. 17 presents a comparison of the computed principal tensile stresses with the strengths measured. The results suggest that the HfB_2 materials will theoretically

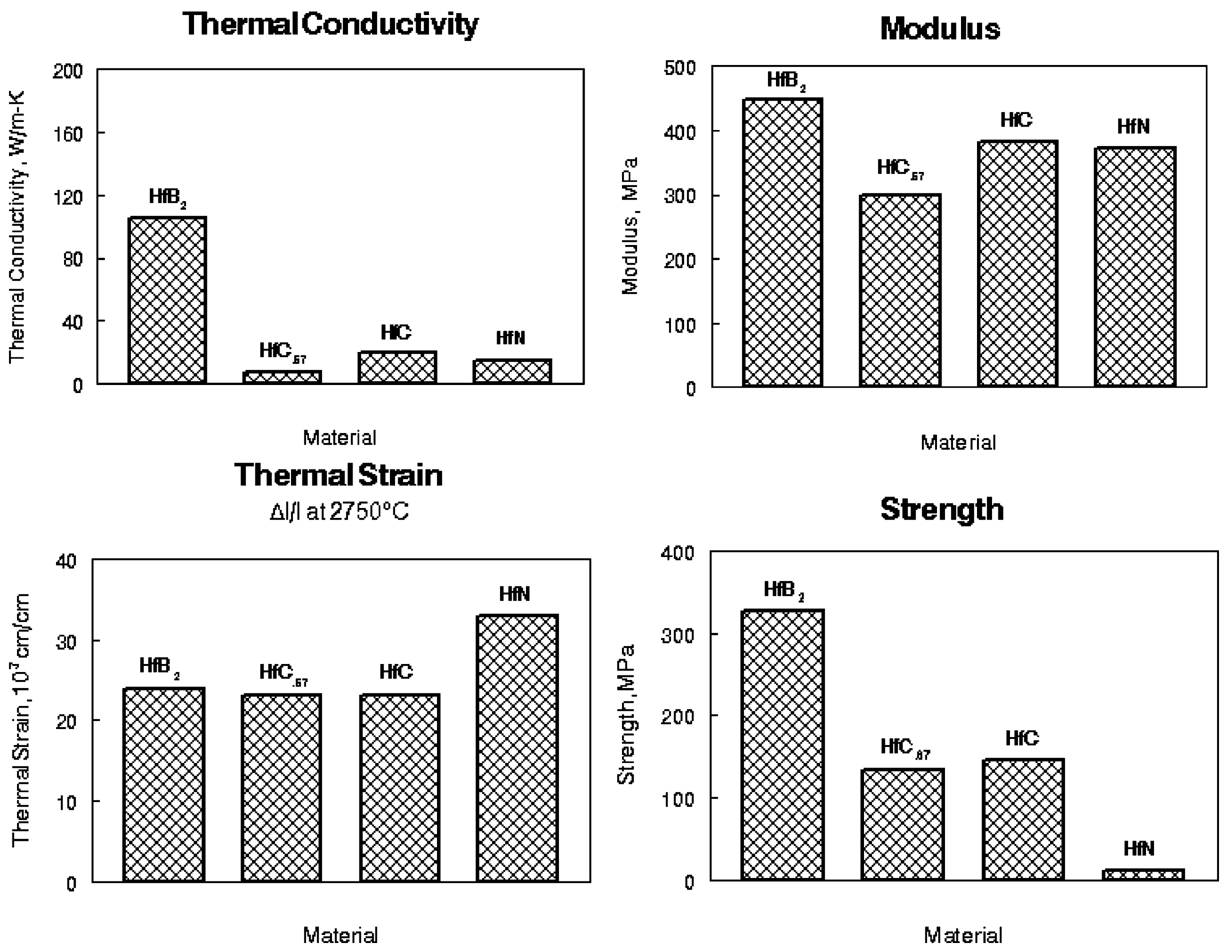

Figure 14 The measured properties of HfB_2, $HfC_{0.67}$, HfC, and HfN used in thermomechanical design model.

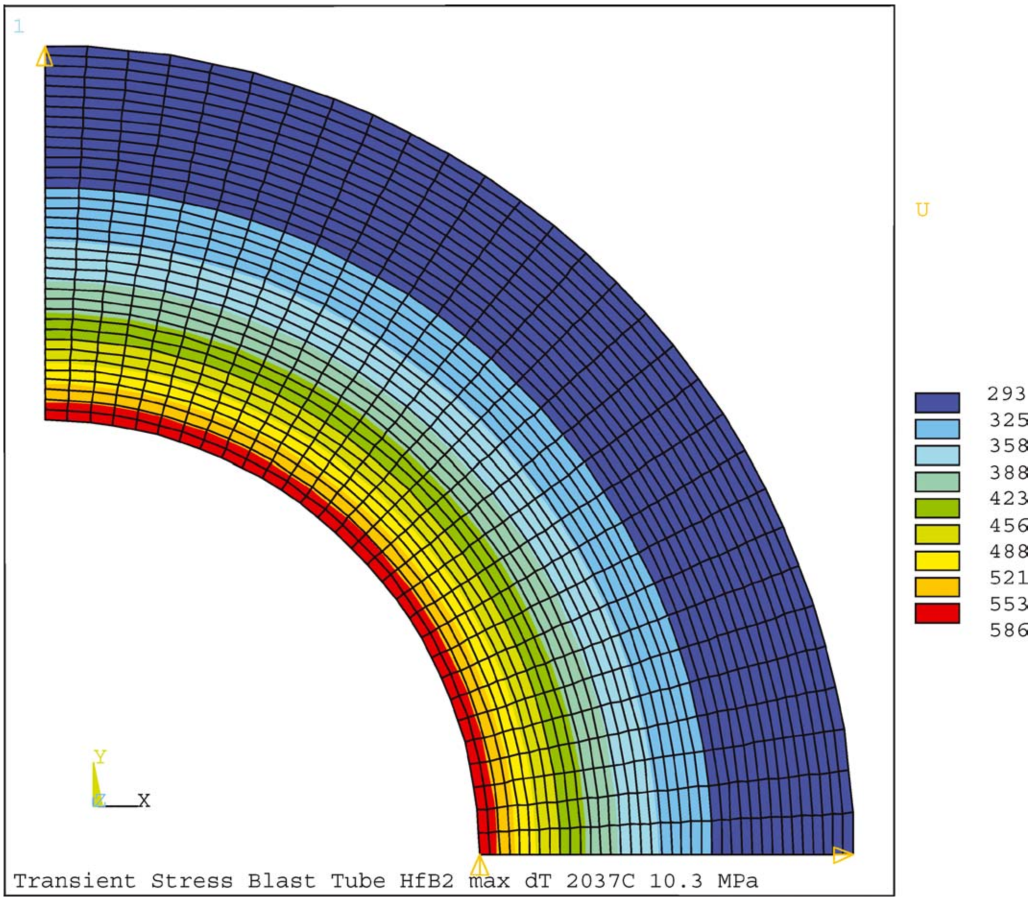

Figure 15 The thermal gradient for wedge specimen from finite element model.

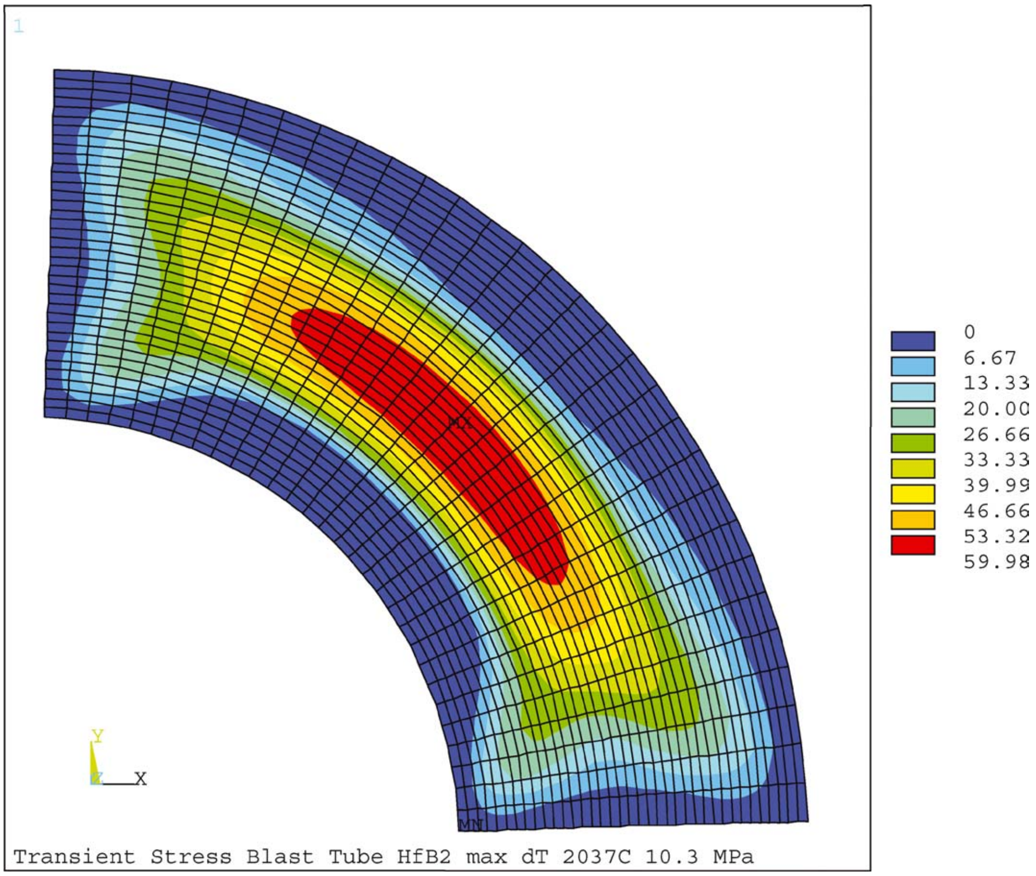

Figure 16 The computed principal stresses in wedge sample from finite element model.

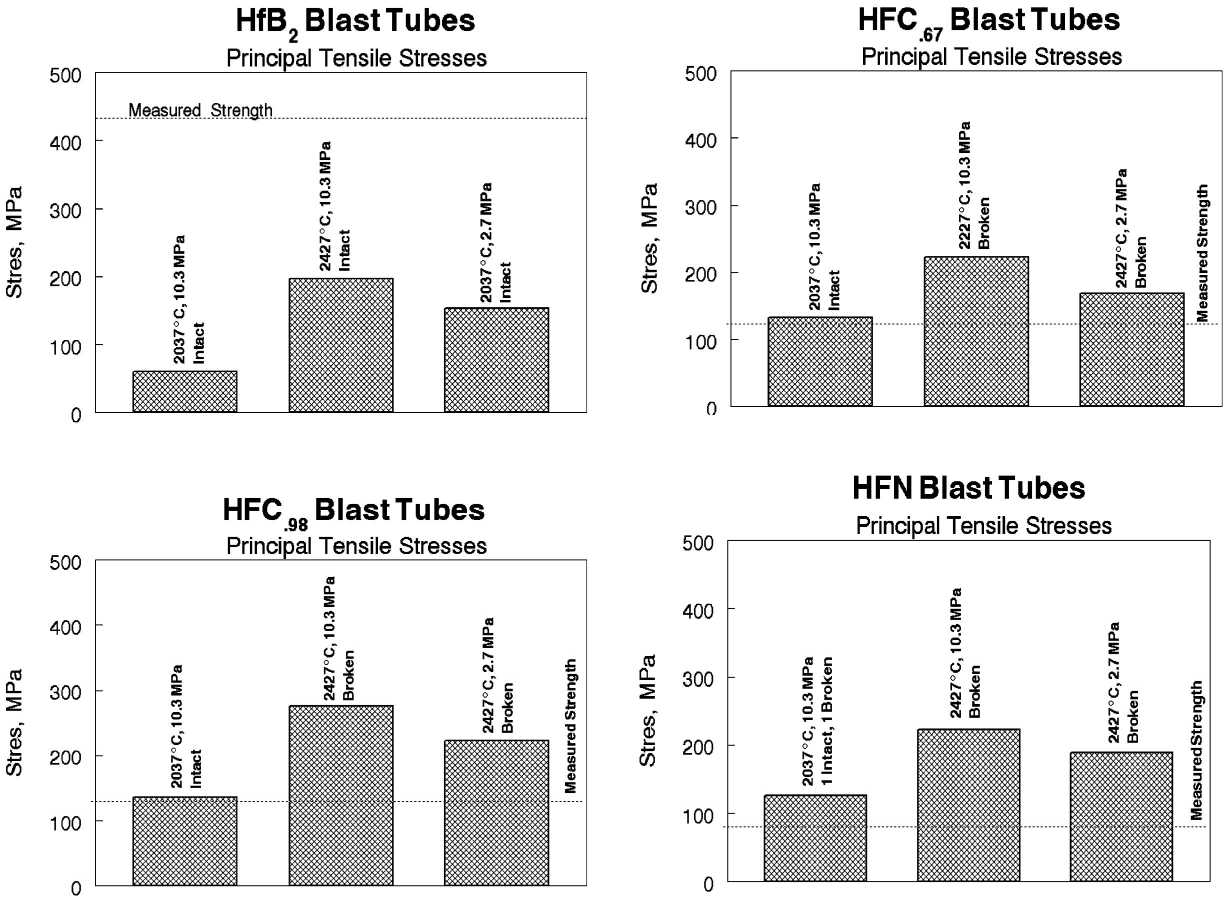

Figure 17 The computed principal stresses at maximum dT plotted for each material at 2037 and 2427°C versus the measured strength showing that HfB_2 should survive all test conditions.

survive both the 2000 and 2400°C conditions, and that the remaining materials will definitely fail in the 2400°C stagnation temperature. Under the 2000°C conditions, the results show that the computed stresses in $HfC_{.67}$, $HfC_{.98}$, and HfN are slightly above the measured strengths. In the nozzle tests, however, some of the test samples survived this condition. This discrepancy may be evidence of two phenomena. First, the materials may exhibit a Weibull strength response and since the blast tube washers are smaller than the SoRI test specimens, the washers may be somewhat stronger. Second, the blast tube specimens reach their failure strain in 1 to 2 s, while the property tests take minutes to reach failure. Thus strain rate effects may act to increase the strength of the blast tube specimens. The overall comparison between the theory and test, however, is seen to give excellent agreement implying that the response of the refractory nozzle materials is well understood.

6. Conclusions

The thermal and mechanical properties of hafnium-based nonoxide ceramics were measured. It was found that modified HfB_2 had a much lower ductile-to-brittle transition temperature than $HfN_{0.92}$ or $HfC_{0.98}$. The effect of lowering the carbon stoichiometry was also to decrease the transition temperature. The thermal conductivity of HfB_2 was much greater (by a factor of 5) than the carbides or nitride. The CTE of all materials tested were approximately the same up to 1500°C, with $HfN_{0.92}$ exhibiting a higher expansion than the others up to 2500°C. The HfB_2 ceramics had the highest modulus of the materials tested, while $HfC_{0.67}$ had the lowest. While the modulus measured during the flexural tests tended to be lower than those measured by the ring and ultrasonic methods, the trends between materials was consistent regardless of the measurement technique. The newer Generation 1 and Generation 2 HfB_2 materials offer improved strength, which should lead to increased design flexibility when using these materials in extreme environments.

Hexagonal α-Hf containing up to 30 at.% N have been prepared, and compression tests were performed to characterize the strength and ductility of the materials. The fracture stress measured at room temperature has a maximum value for 5% N. The brittle-to-ductile transition temperature increases with increasing N content. Stress exponents measured from steady-state compressive deformation up to 1000°C are between 5 and 8, and indicate a dependence on temperature. All experimental results can be interpreted on the basis of dislocation-controlled plasticity with the N (and N clusters) acting as classical solid-solution hardening solutes.

The comparison of theoretical failure calculations with the observed response of refractory materials in rocket nozzle blast tubes has shown good agreement implying that the behavior of the design is well understood. The theoretical model required accurate material properties, realistic thermal boundary conditions, transient heat transfer analysis, and a good understanding of the displacement constraints. The results suggest that a simple thermal strain design criterion is reasonable for thin liners (.050 inch), but too conservative for thicker designs. The understanding gained in this study provides the foundation for advanced nozzle designs including thin liners surrounded by insulating foams, and freestanding ceramic matrix composites.

Acknowledgements

The authors are grateful to S. Fishman of the Office of Naval Research and D. Haught and S. Waslo of the U.S. Department of Energy for providing funding for portions of this program. The authors would also like to acknowledge N. Elsner and A. Metcalfe of Hi-Z Technologies for providing materials for this study.

References

1. H. OKAMOTO, *Bull. Alloy Phase Diagr.* **11**(2) (1990) 146.
2. B. JOHANSSON, J. SUNDGREN and U. HELMERSON, *J. Appl. Phys.* **58**(8) (1985) 3112.
3. O. RUANO and G. ELSSNER, *J. Less Comm. Met.* **52** (1977), 153.
4. E. RUDY and S. WINDISCH, Tech Rep. AFML-TR-65-2 (1966) p. 1.
5. O. KUBASCHEWSKI-VON GOLDBECK, "Phase Diagram*s*" (International Atomic Energy Agency, Vienna, 1981).
6. J.R. FENTER, *SAMPE Quarterly* **2**(3) (1971) 1.
7. L. KAUFMAN and E.V. CLOUGHERTY, AFML-RTD-TDR-63-4096 (1963).
8. D. F. WILEY, W. R. MANNING and O. HUNTER, *J. Less Comm. Met.* **18** (1969) 149.
9. E. RUDY, AFML-TR-65-2 (1969).
10. J. B. BERKOWITZ-MATTUCK *J. Electrochem. Soc.* **113**(9) (1968) 908.
11. W. C. TRIPP and H. C. GRAHAM, *J. Electrochem. Soc. (Solid State Sc.)* **118**(7) (1971) 1195.
12. H. C. GRAHAM *et al.*, in Proceedings of the Sixth University Conference on Ceramic Science, North Carolina State University at Raleigh Dec. 7/9, 1970, Materials Science Research, Vol. 5 (Plenum Press, New York, 1971) p. 35.
13. E. V. CLOUGHERTY, AFML-TR-68-190 (1968).
14. W. C. TRIPP, H. H. DAVIS and H. C. GRAHAM, *Ceram. Bull.* **52**(8) (1973) 612.
15. **D. J. RASKY**, J. D. BULL and H. K. TRAN, in the 15th Conference on Metal Matrix, Carbon, and Ceramic Composites (1991) p. 153.
16. I. G. TALMY, E. J.WUCHINA and J. A. ZAYKOSKI, "Ceramic Matrix Composites" (Materials Research Society, Pittsburgh, PA, 1994).
17. J. L. ROUTBORT, *Acta Metall.* **30** (1982) 663.
18. A. J. PERRY, *Powder Metall. Intern.* **19**(1) (1987) 29.
19. J. P. HIRTH and J. LOTHE, "Theory of Dislocations" (McGraw-Hill, New York, 1968).
20. H. CARSLAW and J. JAEGER, "Conduction of Heat in Solids" (Oxford University Press, London, 1959) p. 112.
21. S. TIMOSHENKO, "Strength of Materials, Part II, Advanced Theory and Problems" (Kreiger, Huntington, NY, 1976).
22. H. SHAPIRO, "The Dynamics and Thermodynamics of Compressible Gas Flow" (Ronald Press, New York, 1953) p. 88.
23. D. BARTZ, *Jet Propulsion* **27** (1957) 49.

Received 24 November 2003
and accepted 16 April 2004